Volume 1 | Number 1 | Jan 2013 | Pages 1–100

Journal of
Materials Chemistry A

Materials for energy and sustainability
www.rsc.org/materialsA

Li⁺

ROYAL SOCIETY
OF CHEMISTRY

ROYAL SOCIETY
OF CHEMISTRY

www.rsc.org/materialsA

Aliovalent Doping of CeO$_2$: DFT-study of Oxidation State and Vacancy Effects.[†]

Danny E. P. Vanpoucke,[*a,b] **Patrick Bultinck,**[a] **Stefaan Cottenier,**[b,c] **Veronique Van Speybroeck,**[b] **and Isabel Van Driessche**[a]

The modification of CeO$_2$ properties by means of aliovalent doping is investigated within the *ab-initio* density functional theory framework. Lattice parameters, dopant atomic radii, bulk moduli and thermal expansion coefficients of fluorite type Ce$_{1-x}$M$_x$O$_{2-y}$ (with M= Mg, V, Co, Cu, Zn, Nb, Ba, La, Sm, Gd, Yb, and Bi) are presented for $0.00 \leq x \leq 0.25$. The relative stability of the doped systems is discussed, and the influence of oxygen vacancies is investigated. It is shown that oxygen vacancies tend to increase the lattice parameter, and strongly decrease the bulk modulus. Defect formation energies are correlated with calculated crystal radii and covalent radii of the dopants, and are shown to present no simple trend. The previously observed inverse relation between the thermal expansion coefficient and the bulk modulus in group IV doped CeO$_2$ [*J. Am. Ceram. Soc.* 97(1), 258 (2014)] is shown to persist independent of the inclusion of charge compensating vacancies.

1 Introduction

Cerium oxide based materials have been receiving increasing attention during the last decades. This is due to their versatile nature in industrial applications, which originate from the remarkable oxidation and reduction properties of CeO$_2$. As such the majority of ceria-based-materials research is linked to solid oxide fuel cells and catalysis.[1–12] In case of the latter, these materials play both the role of catalyst support and catalyst. In addition to being used in automotive three-way-catalyst (TWC) and water-gas-shift reactions, ceria-based-materials are also used as oxygen sensors, thermal barrier coatings and much more.[11–15] CeO$_2$ and doped CeO$_2$ have also been used as buffer layers for thin film YBa$_2$Cu$_3$O$_{7-\delta}$ coated superconductors.[16–22]

In experiments, CeO$_2$ has been doped with many different types of elements.[2,23] These experiments show different dopant elements to have different effects on different properties. Furthermore, based on the application of interest, dopant concentrations can vary from $< 1\%$ up to mixed oxides where dopant concentrations of 50% and more are used. In addition, also the preparation methods vary greatly (*e.g.* combustion synthesis,[24,25] chemical and physical vapor deposition,[26,27] sol-gel deposition[18,21,22] *etc.*), which may have a significant

impact on the investigated properties.[28–32] In contrast to all this variation, ceria-based-materials generally have the same crystal structure (*i.e.* the fluorite crystal structure), adding to their usefulness for general applications.

Although the amount of theoretical work on ceria is significantly smaller than the experimental body of work, it is still extensive. Much of this work focusses on a single aspect of a single application, often investigating the effect of a single dopant element.[7–9,33–42] Investigations of series of dopant elements are much less frequent, and with only few exceptions almost exclusively focus on the lanthanide series.[36,43–46] This is mainly due to the fact that this series (or elements from it) is also the most often investigated in experiments.[2,5,13,22,23,31,32,47–50] Recently, also the series of tetravalent/group IV elements have been investigated by means of *ab-initio* calculations. Andersson *et al.*[51,52] focused on the ionic conductivity of oxygen vacancies in CeO$_2$ doped with tetravalent elements, while Tang *et al.*[53] studied the influence of tetravalent dopants on the redox properties of CeO$_2$. The present authors investigated the stability and influence of group IV dopants on mechanical and structural properties of CeO$_2$.[54,55]

With the large variety of applications comes a large variation in desired properties. The optimal value for one and the same property may even be opposite for different applications: *e.g.* for a system to be a good solid oxide fuel cell, it should exhibit high ionic conductivity, whereas for it to be a good buffer layer, it should have a low ionic conductivity. A second example: lattice matching through doping of a buffer layer requires a homogenous distribution of the dopants in the bulk of

[a] Department of Inorganic and Physical Chemistry, Ghent University, Krijgslaan 281 - S3, 9000 Gent, Belgium. E-mail: Danny.Vanpoucke@Ugent.be
[b] Center for Molecular Modeling, Ghent University, Technologiepark 903, 9052 Zwijnaarde, Belgium.
[c] Department of Materials Science and Engineering, Ghent University, Technologiepark 903, 9052 Zwijnaarde, Belgium.
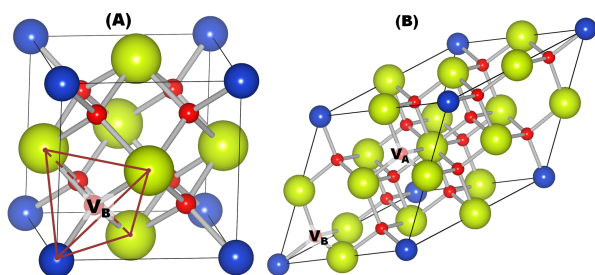
Fig. 1 (color online) Ball-and-stick representations of doped CeO_2 c111 (a) and p222 (b) supercells. Yellow (red) spheres indicate the positions of the Ce (O) atoms, while the dopant position is given by the blue sphere. Vacancy positions are indicated (V_A and V_B), as is the surrounding tetrahedron (red lines). The single dopant/oxygen vacancy gives rise to a dopant/vacancy concentration of 25%/12.5% in the c111, and 12.5%/6.25% in the p222 supercell, respectively.

Fig. 2 (color online) Ball-and-stick representations of different $Ce_{0.75}Gd_{0.25}O_{1.875}$ configurations in a double c111 supercell. Yellow, red, and purple spheres indicate the positions of the Ce, O, and Gd atoms. Possible vacancy positions are indicated (V_A, V_B, and V_C).

the material, while catalysts often benefit from dopants residing at or near the surface.

With this in mind, this work aims at presenting general trends for doped ceria, and does not focus on either one specific application or one specific dopant. This paper extends our previous work through the study of aliovalent dopants, and the introduction of charge compensating vacancies.[55,56] For practical reasons we have limited our work to a subset of the aliovalent dopants investigated in experimental work: Mg, V, Co, Cu, Zn, Nb, Ba, La, Sm, Gd, Yb, and Bi.[2,3,13,20–25,47,50,57–77]

In this paper, we investigate the influence of aliovalent doping on the properties of CeO_2 using *ab-initio* density functional theory (DFT) calculations. The theoretical methods and different supercells used are presented in Sec. 2. To study the contributions due to the dopants and vacancies separately, we first consider systems containing dopants only (Sec. 3), and then systems containing combinations of dopants and charge compensating oxygen vacancies (Sec. 4). For systems without oxygen vacancies, the atomic radii of the dopants are calculated and compared to the values tabulated as the Shannon atomic crystal radii.[78,79] Concentration dependent defect formation energies are calculated and put in relation to the calculated dopant radii and covalent dopant radii. The change in the bulk modulus (BM) and thermal expansion coefficient (TEC) of CeO_2 due to the dopants is studied, and it is shown that the BM and TEC follow opposite trends. In addition, we investigate the modification, due to charge compensating vacancies, of the dopant (Cu, Zn, and Gd) influence on the BM, defect formation energy and lattice parameter. Summary and conclusions are presented in Sec. 5.
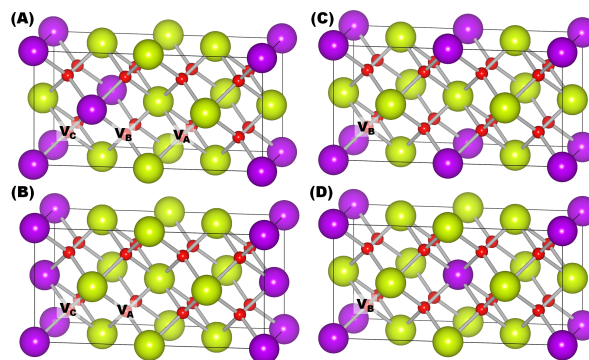
2 Computational setup

We perform *ab-initio* density functional theory (DFT) calculations using the projector augmented waves (PAW) method as implemented in the Vienna *ab-initio* Package (VASP) program. The LDA functional as parameterized by Ceperley and Alder and the GGA functional as constructed by Perdew, Burke and Ernzerhof (PBE) are used to model the exchange and correlation behavior of the electrons.[80–86] The plane wave kinetic energy cutoff is set to 500 eV.

To optimize the structures, a conjugate gradient method is used. During relaxation both atom positions and cell-geometry are allowed to change simultaneously. The convergence criterion is set to the difference in energy between subsequent steps becoming smaller than 1.0×10^{-6} eV.

Because this work focusses on general trends in the properties of doped CeO_2 as function of dopant concentration, we assume the dopants to be distributed homogeneously in an ordered fashion. This allows for the investigation of a wide range of concentrations going from about 3 % up to 25 %. In specific cases, doped systems are known to show clustering or disordered distributions of the dopants, often depending on the actual dopant concentration and the method of synthesis.[28,38,87] As such, small deviations from the presented results are to be expected in experiments. In Sec. 2.1 and 2.2 the supercells used for systems with and without vacancies are presented.

The TEC is calculated as the numerical derivative of V(T) data, which is obtained from the minimization of the thermal non-equilibrium Gibbs function. The latter is calculated using the quasi-harmonic Debye approximation,[88–90] and is implemented as a module in our in-house developed HIVE code.[91]

The BM is calculated by fitting E(V) data from fixed volume calculations to the third order isothermal Birch-Murnaghan equation of state. [92,93]

The accurate description of the electronic structure of reduced ceria (CeO_{2-x} and Ce_2O_3) is a well known issue for regular DFT approaches. [94,95] It is closely related to the localized nature of the Ce $4f$ electron. To correctly model the strong on-site Coulomb repulsion of the Ce $4f$ electron in reduced ceria, a tunable Hubbard type correction term can be included into the DFT framework: DFT+U. This tunable U is generally obtained from fitting to experimental data (*e.g.* band gap width). For reduced ceria several theoretical studies exist where a wide range of U values is scanned, leading to the suggestion of U=5–6 eV for LDA, and U=4–5 eV for GGA functionals. [95–98] Most of these studies focus on the accurate description of the electronic structure near the band gap. It is, however, interesting to note that the optimum U depends on the property investigated. This is because an important side effect of the standard DFT+U formalism is the fact that many properties (lattice parameter, band gap, formation energy,...) vary with the value of U. [95–99] Despite the issues with the electronic structure of reduced ceria, regular DFT describes the crystal structure and electronic structure of pure CeO_2 accurately (LDA slightly underestimates the lattice parameter, while PBE overestimates it slightly). [96,98–101] In previous work, it was shown that the formation energies of CeO_2 doped with group IV elements remains qualitatively unchanged, while for $La_2Ce_2O_7$ the lattice parameters and relative stability showed the same behavior for regular DFT as for DFT+U. [38,55] Also for ionic migration and defect association in Sm and Gd codoped CeO_2 it was shown that regular DFT presents qualitatively accurate results. [46]

In Table 1 DFT, DFT+U, and experimental values of the properties of interest in this work are compared for pure CeO_2 and $Ce_{0.75}Gd_{0.25}O_2$. In the DFT+U calculations, a U= 5.0 eV for the Ce $4f$ electrons and U= 6.7 and J= 0.7 eV for the Gd $4f$ electrons is used, in accordance with the values suggested for these materials in literature. [95–99,102,103] The results presented in Table 1 show DFT and DFT+U to give qualitatively the same results, with variations due to the +U correction that are (much) smaller than those resulting from the use of different functionals. Furthermore, all calculated values are in good agreement with the experimental values.

As such, since the current work does not focus on the electronic structure (which is sensitive to small changes in geometry, topology and stoichiometry) but instead focusses on the structure (lattice parameter) and derived mechanical properties (bulk modulus and thermal expansion coefficients), we make the pragmatic choice of not going beyond the LDA/PBE level of theory.

2.1 Non-vacancy systems

Symmetric supercells, containing a single dopant per cell are used to simulate a homogeneous distribution of dopant ions without charge compensating vacancies. [56] For each system, structural optimization is started from the fluorite geometry (space group $Fm\bar{3}m$), maintaining the crystal symmetry. The supercells used are the fluorite cubic $1 \times 1 \times 1$ cell with 12 atoms (c111), the primitive $2 \times 2 \times 2$ cell with 24 atoms (p222), the primitive $3 \times 3 \times 3$ cell with 81 atoms (p333) and the cubic $2 \times 2 \times 2$ cell with 96 atoms (c222). Replacing a single Ce atom with a dopant element results in dopant concentrations of $25, 12.5, 3.7037$, and 3.125 %, respectively. The doped c111 and p222 supercells are shown in Fig. 1, with the dopant element position indicated by the blue spheres.

Monkhorst-Pack special k-point grids are used to sample the Brillouin zone: [116] an $8 \times 8 \times 8$ k-point grid for the two smaller cells, and a $4 \times 4 \times 4$ k-point grid for the two large supercells.

2.2 Systems containing compensating oxygen vacancies

For doped systems containing a single oxygen vacancy, only the c111 and p222 supercells are used, giving rise to dopant concentrations of 25 and 12.5%, respectively, and oxygen vacancy concentrations of 12.5 and 6.25%, respectively. The c111 and p222 configurations are shown in Fig. 1, where possible oxygen vacancy positions are labeled V_A and V_B (*cf.* further). Every oxygen atom is positioned at the center of a cation-tetrahedron, as is shown in Fig. 1. As a result, every vacancy site can have up to four dopant atoms as nearest neighbor. For calculations containing two dopants and one vacancy a double c111 supercell is used, this to retain the crystal structure of our 25 % doped model, allowing for direct comparison. Four inequivalent dopant distributions (A, B, C, and D) are used, shown in Fig. 2. To investigate the influence of oxygen vacancies, a homogeneous distribution of the vacancies is assumed, similar as for the dopants. For low oxygen vacancy concentrations, we assume that results for random distributions of vacancies (*e.g.* Ref. [38,103]) can be approximated as linear combinations of the configurations presented here. However, to retain a clear image of the specific influence different configurations have, only these homogeneous distributions of vacancies are investigated. Effects due to clustering are beyond the scope of this work as they are dopant and synthesis method dependent, and as such will not be treated. Note however, that such clustering may lead to deviations in the experimentally obtained results when compared to the theoretical results presented in this work.

In this work vacancy sites with 0 neighboring dopants are indicated as V_A, while configurations with 1 or 2 dopants in the surrounding tetrahedron are indicated as V_B and V_C, re-

Table 1 Comparison of DFT and DFT+U.[a]

| | CeO$_2$ | | | | | Ce$_{0.75}$Gd$_{0.25}$O$_2$ | | Ce$_{0.8}$Gd$_{0.2}$O$_{1.9}$ |
	LDA	LDA+U	PBE[e]	PBE+U	exp.	PBE[e]	PBE+U	exp.[d]
E$_f$(eV)	−11.484	−11.641	−10.418	−10.493	−10.44/−11.30[b]	2.396	2.664	
a$_0$ (Å)	5.362	5.394	5.463	5.488	5.406/5.411[b]	5.468	5.497	5.419/5.429
B$_0$ (Mbar)	2.014	2.094	1.715	1.803	2.04/2.36[b]	1.588	1.654	1.60/1.77
α (10^{-6} K^{-1})	11.214	10.577	12.953	12.040	10.7/12.68[c]	13.753	12.839	11.59/13.3

[a] E$_f$: Calculated defect formation energy for Ce$_{0.75}$Gd$_{0.25}$O$_2$ and heat of formation for CeO$_2$, a$_0$: the lattice parameter, B$_0$: bulk modulus, and α: linear thermal expansion coefficient, calculated at 500 K.
[b] Taken from references [96–98,101,104–108] and references therein.
[c] Taken from references [109,110] and references therein.
[d] Taken from references [46,111–114] and references therein.
[e] In the work of Lejaeghere et al. [115] general error bars for PBE derived materials properties were calculated based on pure materials (single atomic species, excluding lanthanides and actinides). Assuming these error bars can be transferred to Lanthanide based oxides, the error bar on B$_0$ would be 0.15 Mbar, and the error bar on a$_0$ would be about 2.5%.

spectively (*cf.* Figs. 1 and 2). Because only single oxygen vacancies are present, all Ce atoms in each of the systems will either be 7-or 8-coordinated.

Similar as for the supercells without vacancies, Monkhorst-Pack special $k-$point grids of $8 \times 8 \times 8$ grid points are used for the c111 and p222 cells. [116] For the double c111 supercells a $4 \times 8 \times 8$ grid is used instead.

3 Aliovalent dopants without compensating oxygen vacancies

The use of aliovalent dopants in CeO$_2$ introduces two (related) complications from the theoretical point of view. Firstly, aliovalent dopants give rise to charge compensating vacancies, which increases the number of possible configurations per dopant concentration significantly if the ground state configuration is unknown. Secondly, since many elements can have multiple oxidation states this introduces additional uncertainties with regard to the number of required compensating vacancies and thus the ground state crystal structure.

For these reasons, we start by investigating uncompensated dopants in fluorite Ce$_{1-x}$M$_x$O$_2$ with M=Mg, V, Co, Cu, Zn, Nb, Ba, La, and Bi. This has the advantage that only effects directly due to the aliovalent dopants are observed. In Sec. 4 compensating vacancies are added. This approach allows us to discriminate between dopant and oxygen vacancy induced changes of the investigated property. In addition, the uncompensated situation can be physically interpreted as doped systems under highly oxidizing atmosphere, which may be of interest for catalytic processes in for example automotive TWC. [2,4,11,117,118]

3.1 Lattice parameters, dopant radii and Vegard's law

In previous work, it was shown that for cubic systems without oxygen vacancies the radius of the dopant element can be calculated as: [54,55]

$$R_M = \left(\frac{\sqrt{3}}{4}a_{Ce_{1-x}M_xO_2} - R_O - (1-n_x)R_{Ce}\right)/n_x, \quad (1)$$

with n_x the dopant concentration, $a_{Ce_{1-x}M_xO_2}$ the lattice parameter of the doped system, and R_O and R_{Ce} the radii of O and Ce, respectively. From this the empirical Vegard law was obtained. [54,119] In doping experiments, lattice parameters are often linearly fitted with regard to the dopant concentration. Deviation with respect to this Vegard law behavior is interpreted as an indication of the presence of secondary phases, phase transitions or saturation, depending on the observed deviation. [22,47,50,65,73,120,121]

Table 2 shows the calculated dopant radii and coefficients of Vegard's Law. The intercept a and slope b of this linear relation are found by rewriting Eq. (1) as

$$a_{Ce_{1-x}M_xO_2} = a_{CeO_2} + \left(\frac{4}{\sqrt{3}}(R_O + R_M) - a_{CeO_2}\right)n_x, \quad (2)$$

as is shown elsewhere. [54] The small standard deviations on the calculated dopant radii (≤ 0.01Å) show consistent values are found for the systems with different concentrations. The calculated lattice parameter for Ce$_{0.75}$Sm$_{0.25}$O$_2$ seems to be in good agreement with the experimental lattice parameter of 5.4314Å for Ce$_{0.8}$Sm$_{0.2}$O$_{2-\delta}$ by Yao et al. [77] and ~ 5.435Å for Ce$_{0.85}$Sm$_{0.15}$O$_{1.925}$ by Xu et al. [76], knowing that PBE generally overestimates lattice parameters by a few percent. Also the very small variation of the experimental lattice parameter with the Sm concentration is in qualitative agreement with the calculated slope of the Vegard law, if one takes into account

Table 2 Dopant radii and Vegard law for aliovalent dopants[a]

	R_M (Å)				Vegard's Law				LDA		PBE	
	LDA		PBE		LDA		PBE		a_0	a_{RT}	a_0	a_{RT}
	avg	stdev	avg	stdev	a(Å)	b	a(Å)	b	(Å)	(Å)	(Å)	(Å)
CeO_2	1.0819^b	0.0001	1.1257^b	0.0004					5.362	5.388	5.463	5.492
Mg	0.958	0.008	1.022	0.011	5.364	−0.315	5.465	−0.273	5.285	5.316	5.396	5.432
V	0.823	0.005	0.870	0.005	5.363	−0.613	5.464	−0.610	5.209	5.235	5.312	5.341
Co	0.883	0.005	0.949	0.007	5.363	−0.478	5.464	−0.427	5.243	5.273	5.357	5.392
Cu	0.913	0.002	0.991	0.006	5.362	−0.395	5.463	−0.307	5.264	5.299	5.387	5.428
Zn	0.952	0.005	1.028	0.008	5.363	−0.317	5.464	−0.239	5.283	5.315	5.404	5.440
Nb	0.926	0.005	0.961	0.005	5.363	−0.375	5.464	−0.395	5.269	5.292	5.365	5.392
Ba	1.332	0.003	1.403	0.001	5.363	0.566	5.464	0.635	5.504	5.533	5.622	5.656
La	1.186	0.001	1.242	0.004	5.362	0.237	5.464	0.260	5.422	5.448	5.529	5.559
Sm	–	–	1.169	0.004	–	–	5.464	0.095	–	–	5.487	5.517
Gd	–	–	1.139	0.005	–	–	5.464	0.015	–	–	5.468	5.498
Yb	–	–	1.104	0.008	–	–	5.464	−0.056	–	–	5.449	5.482
Bi	1.107	0.003	1.165	0.009	5.363	0.044	5.465	0.060	5.373	5.400	5.480	5.511

[a] Dopant radii calculated using Eq. (1), averaged over the four dopant concentrations (avg), and standard deviation (stdev) of this value. This is done for both LDA and PBE calculated geometries. a and b are the intercept and slope of Vegard's law linear fit (*cf.* Eq. (2)) to the calculated geometries for doped CeO_2 systems. Lattice parameters at zero Kelvin a_0 and room temperature (RT) a_{RT} (300 K) are given for $Ce_{0.75}M_{0.25}O_2$. The CeO_2 values are given as reference.[86]
[b] The Ce radius is calculated using Eq. (1), where the 4-coordinated Shannon crystal radius for oxygen is taken as 1.24 Å[78,79].

that the different synthesis methods have an influence on the obtained lattice parameters.[76,77] Yao *et al.* also calculated the Vegard law slope for Co doped $Ce_{0.8}Sm_{0.2}O_{2−δ}$ and find a lattice contraction, in qualitative agreement with our theoretical results.[77] The smaller experimental lattice contraction is mainly due to the presence of oxygen vacancies. As will be shown in Sec. 4.2.2, oxygen vacancies give rise to a lattice expansion relative to a system without oxygen vacancies. As such, they compensates the lattice contraction due to the Co dopants to some extent, lowering the degree of lattice contraction.

The obtained lattice parameters for Gd, Sm and La also agree well with the theoretical work of Wang *et al.*[103] In their study, the authors made use of special quasi random structures to model disordered systems with dopant and oxygen vacancy concentrations ranging from 19 to 25 % and 5 to 6 %, respectively. Their obtained lattice parameters are about 1–2 % larger than those presented in Table 2, due to both the presence of oxygen vacancies (as will be shown in sec. 4.2.2) and the use of a DFT+U formalism. Using the slope and intercept obtained for Sm and Gd doped CeO_2, perfect agreement is found with the theoretical work of Alaydrus *et al.*[46] Note that although the systems of these authors contain oxygen vacancies, their concentration (1.56 %) is so low that their contribution to the lattice expansion is negligible (*cf.* sec. 4.2.2: for Gd the vacancy contribution can be estimated to be about $4 \times 10^{−4}$ Å). The calculated slopes for Gd and Sm doped CeO_2 are also in

good agreement with the experimental work of Wang *et al.*[122] They observe Vegard law behavior with slopes of 0.0813 and 0.134 for Gd and Sm respectively. These values are somewhat larger than those presented in Table 2, which is to be expected due to the presence of oxygen vacancies in the experimental samples.

In Fig. 3 the calculated atomic radii are compared to the Shannon crystal radii for 6-,7-, and 8-coordinated configurations.[78,79] For tetravalent V and Nb, both LDA and PBE results are in good agreement with the 8-coordinate Shannon crystal radius, and also the radii for divalent Mg and Zn show good agreement with the 8-coordinate radii.[123] For the trivalent lanthanides on the other hand, the calculated radii in this 8-coordinated environment agree better with tabulated Shannon radii for lower coordination. This is also the case for trivalent Bi and monovalent Cu. This may suggest a tendency for these elements to prefer a lower than 8-coordination. If this is the case, then in experiments with these specific dopants significant structural reconstructions in the environment of the dopant are to be expected (including but not necessarily the presence of oxygen vacancies). For Cu this is in good agreement with the coordination number 5–6 obtained by Wang *et al.* from X-ray adsorption fine structure (XAFS) measurements.[59] Lu *et al.*[37], however, found a 4-coordination in their calculations, where a broken symmetry structure for the Cu doped CeO_2 was used. The resulting tetragonal structure for such a broken symmetry system is 0.667% larger in volume

than the cubic fluorite structure used in this work, making the calculated atomic radius for Cu slightly larger than the one presented. The value for divalent Co in turn tends toward 7-fold coordination. Note that the Shannon crystal radii for Co^{III} and Co^{IV} would be too small,[78,79] showing that the divalent nature, inferred from the calculated radius, supports the experimental suggestion of divalent Co dopants.[30,69,72–74,124]

The results for Ba are a bit peculiar, since the calculated radius is significantly lower than either 6-, 7-, or 8-coordinate Shannon crystal radii for divalent Ba.[78,79] Assuming the general trends seen in the Shannon crystal radii for other elements are also valid for Ba (i.e. increasing valence results in decreasing radius under constant coordination) this would lead to the conclusion that Ba behaves as having an oxidation state higher than II when used as a substituent for CeO_2, which is puzzling.

In conclusion, in contrast to our previous work on group IV elements, we observe 8-coordinated aliovalent dopants to act as if they are undercoordinated.[54,55] This may indicate that many aliovalent dopants will give rise to local deformations of the crystal structure, in order to effectively realize such undercoordination. Dopant-vacancy complexes are one example, but also square planar reconstructions of the dopant-oxide environment may be expected for mono-and divalent (*d*-block) elements (*cf.* the case of Cu).

On the other hand, as might be expected, perfect Vegard law behavior is found for all the systems under investigation. Combined with the calculated atomic radii, this provides a way to *estimate* the valence of dopant elements in experiments, based on the obtained lattice parameter under oxidizing atmosphere:

1. Calculate the atomic crystal radius of the dopant, R_M, based on the measured lattice parameter.(*cf.* Eq. 1)

2. Compare R_M to the tabulated values by Shannon.[78,79]

3. The best fit between calculated and tabulated atomic crystal radius provides an estimate for the dopant valence.

It is important to note that this scheme only provides an estimate for the valence/coordination in an experiment based on the lattice parameter. Depending on the actual system the result may be inconclusive or be open to interpretation for several reasons: *e.g.* (i) missing tabulated data (*e.g.* the Ba results in this work),(ii) overlap in the tabulated data (the calculated R_M matches several coordination-oxidation sets equally well), (iii) lack of accurate experimental lattice parameters, (iv) the presence of oxygen vacancies (as will be shown in Sec. 4.2, oxygen vacancies lead to an expansion of the lattice relative to system without vacancies, which in turn will lead to an overestimation of the calculated atomic radius) and, (v) clustering of defects. However, combined with additional experimental knowledge (e.g. X-ray Photoelectron spectroscopy) this
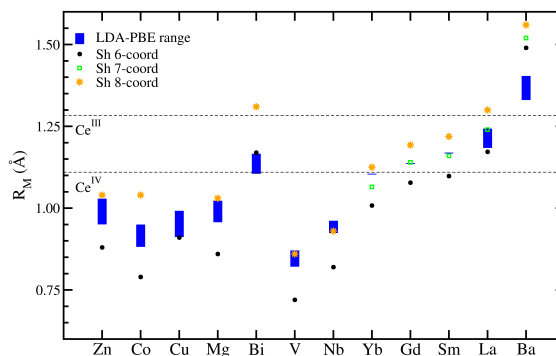

Fig. 3 Comparison of calculated dopant radii in $Ce_{1-x}M_xO_2$ to the Shannon crystal radius for $M=Mg^{II}$, V^{IV}, Co^{II}, Cu^{I}, Zn^{II}, Nb^{IV}, Ba^{II}, La^{III}, Sm^{III}, Gd^{III}, Yb^{III}, and Bi^{III} with coordination numbers 6, 7, and 8 (where available).[78,79] The top of the boxes coincides with the PBE values, while the bottoms indicate the LDA values. Where no LDA values exist, the calculated PBE values are indicated as a blue dash.[86] The dopant elements are sorted according their Covalent radius, with Zn the smallest and Ba the largest element.[125] The Shannon crystal radii for 8-coordinate Ce^{III} and Ce^{IV} are indicated with dashed lines.[78,79]

scheme could lead to conclusive results, which could not be obtained by either method independently.

3.2 Defect formation energies

The stability of the doped systems is investigated through the comparison of the defect formation energy E_f defined as:

$$E_f = E_{Ce_{1-x}M_xO_2} - E_{CeO_2} + N_{df}(E_{Ce} - E_M), \qquad (3)$$

with $E_{Ce_{1-x}M_xO_2}$ the total energy of the doped system, E_{CeO_2} the total energy of a CeO_2 supercell of equal size, N_{df} the number of dopant atoms, and E_{Ce} and E_M the bulk energy per atom of α-Ce and the bulk phase of the dopant element M. Positive values indicate the amount of energy required to substitute a single Ce atom by a dopant.

Defect formation energies given in Table 3 show the same qualitative behavior for the LDA and PBE calculations. Furthermore, as was observed for group IV dopants, formation energies show only limited dependence on the dopant concentration.[55] The results in Table 3 also show that only Sm doping is stable in an absolute sense with regard to segregation into CeO_2 and bulk Sm. This is in line with the DFT+U study of Sm doped CeO_2 by Ismail *et al.*[126] The positive defect formation energy for the other dopant elements indicates a threshold exists for the formation of these compounds. All dopants presented in this work have been used in experiments, and of several a $Ce_{1-x}M_xO_{2-y}$ phase is experimentally observed.[2,3,13,20–25,47,50,57–77] However, in contrast to the

Table 3 Defect formation energy E_f for doped CeO_2 at different dopant concentrations. [86]

	E_f(eV)			
	25%	12.5%	3.704%	3.125%
	LDA			
CeO_2	-11.484^a			
Mg	8.221	8.409	8.470	8.475
V	6.243	6.313	6.338	6.322
Co	12.353	12.425	12.479	12.473
Cu	13.517	13.464	13.463	13.458
Zn	11.465	11.651	11.696	11.707
Nb	3.738	3.445	3.400	3.415
Ba	7.621	7.777	7.933	7.956
La	2.403	2.389	2.418	2.422
Bi	7.902	8.069	8.114	8.095
	PBE			
CeO_2	-10.418^a			
Mg	8.036	8.223	8.275	8.284
V	6.256	6.320	6.348	6.361
Co	11.750	11.780	11.800	11.801
Cu	12.922	12.878	12.878	12.879
Zn	11.057	11.249	11.282	11.300
Nb	4.059	3.746	3.726	3.761
Ba	7.518	7.681	7.850	7.882
La	2.438	2.429	2.464	2.469
Sm	-2.181	-2.218	-2.228	-2.236
Gd	2.396	2.445	2.449	2.448
Yb	4.438	4.495	4.508	4.500
Bi	7.912	8.069	8.111	8.093

^{a} Instead of the defect formation energy the heat of formation is given.

above calculations, experiments are not performed at zero atmosphere and zero Kelvin, and often involve one or more steps that introduce additional energy into the system, providing a means to overcome energy barriers. In addition, the experimental compounds also contain charge compensating vacancies, that are not included in the systems presented in this section. In Sec. 4, we will show that the inclusion of such vacancies has only limited influence on the formation energies, allowing the presented defect formation energies to be used as initial indicators of the system stability.

Since the formation energies presented in Table 3 spread over quite a wide range it is obvious that not all dopants will form a compound system equally easily. In consequence, a reference energy is needed to indicate which are more likely to form a doped bulk phase and which dopants are more likely to segregate either to the surface of the nanocrystals or imbedded clusters. It is well-known for CeO_2 to spontaneously form oxygen vacancies, so the oxygen vacancy formation energy of pure CeO_2 can be used as a reference for the likelihood of

forming a $Ce_{1-x}M_xO_2$ bulk-phase. [2,23] Table 5 shows the calculated oxygen vacancy formation energy for $CeO_{1.96875}$ to be 4.035 and 3.097 eV for LDA and PBE, respectively, going up to 5.006 and 4.145 eV in $CeO_{1.75}$. From this we conclude that Nb and the lanthanides presented in this work are likely to form fluorite based bulk-phases of $Ce_{1-x}M_xO_2$, while the other dopants are expected to segregate either into internal domains or to the surface of the grains.

Combined with the calculated dopant radii of Table 2, a high defect formation energy and a crystal radius indicative of a preference for lower coordination points toward the possibility for local reconstructions around the dopant to be present in experiment. Such reconstructions lead to a better suited chemical environment, with better matched coordination and lower defect formation energies.

Of all dopants presented in this work, Cu shows the highest formation energy, making it the most likely candidate for phase segregation and/or reconstruction. The existence of such a reconstruction is shown in the work of Wang *et al.*[59] and Lu *et al.*[37] where a symmetry breaking reconstruction for the Cu dopant was found and investigated. But even when this reconstructed structure is taken into account, Cu doped CeO_2 remains one of the most unstable systems. The tetragonal reconstruction is only 1.223 eV more stable than the cubic fluorite structure, resulting in a defect formation energy of about 11.7 eV in PBE calculations. In the literature several experimental groups have investigated CuO doped/modified CeO_2 showing a general trend of phase segregation for medium to high Cu content. [24,57–60,66,67,127] Kundakovic and Flytzani-Stephanopoulos investigated the reduction characteristics of CuO dispersed on $Ce_{1-x}La_xO_2$ catalyst supports. [57,58] They found that for low Cu content, copper is present as small clusters or even isolated ions. For higher concentrations, also CuO particles are observed. [57] Similar observations have been reported by Lin *et al.* and also de Biassi and Grillo present evidence of Cu clustering. [66,127] In addition, Kundakovic and Flytzani-Stephanopoulos also present the observation of bulk doped $Ce_{0.99}Cu_{0.01}O_{2-y}$ for calcination temperatures below 500°C, and state that for higher calcination temperatures the Cu ions segregate to the surface to form clusters. This supports the instability of Cu doped CeO_2 predicted by our calculated formation energies.

In contrast, Bera *et al.* do not observe any CuO related lines in their X-ray diffraction spectra for $3-5\%$ Cu doping, nor do they observe CuO particles in their TEM measurements. As a result they conclude Cu ions to be present in the CeO_2 crystal matrix. However, they also note that there are 4 to 6 times as many Cu ions located on the surface of the CeO_2 particles. [24] Combined with the results for low calcination temperatures of Kundakovic and Flytzani-Stephanopoulos this would appear to indicate that a significant kinetic barrier is present for the Cu ions, limiting the mobility of the Cu ions, which in turn

also limits their ability to cluster and/or segregate to the surface after their initial dispersal in the CeO_2 bulk during (for example) high temperature treatment.

Co bulk-doping, on the other hand, which is shown in Table 3 to be almost as unfavorable as Cu doping, is widely used in experimental studies in the context of dilute semiconductors. In many of these experiments, samples which are often thin films, are prepared via pulsed laser deposition.[69,70,72] Observation of $Ce_{1-x}Co_xO_{2-y}$ in these samples may be an indication that high kinetic barriers are present, effectively pinning the Co ions at their initial position despite the unfavorable energetics. Alternatively, Co may segregate into very small Co/CoO clusters, which could at higher Co concentrations give rise to the Co_3O_4 impurities observed by Sacanell et al.[75] This would be in agreement with the XPS results of Ali et al.,[30] which indicate Co not to be present in metallic form. It would also be in line with the calculated preference of oxygen vacancies to reside near Co ions.[128] Yao *et al.* investigated the codoping of Co and Sm in CeO_2 and observed no secondary CoO or Co_3O_4 phases.[77] Combined with the observed Vegard law behavior for Co doping, they conclude that the Co ions are incorporated into the ceria lattice forming a solid solution. This seems to indicate that the codoping with Sm in this case stabilizes the Co dopants somewhat, which is not unreasonable based on the Sm defect formation energy given in Table 3. In addition, Yao *et al.* also observe the grain boundary conductivity to show a maximum at 5% of Co doping.[77] They link this to the segregation of Co to the grain boundary, showing that the Sm dopants can only stabilize a limited amount of Co.

Of the dopants investigated in this work, Ba shows the largest decrease in defect formation energy with increasing concentration. Combined with its relatively large defect formation energy this could indicate that the $BaCeO_3$ interface observed between superconducting $YBa_2Cu_3O_{7-\delta}$ thin films and CeO_2 buffer layers is rather due to Ce moving into BaO layers than Ba moving into the CeO_2 buffer layer.[19,129] On the other hand, if there are Ba atoms that diffuse into a CeO_2 buffer layer, then doping the CeO_2 buffer layer using dopants that have a lower defect formation energy may prevent the Ba diffusion by occupying and thus blocking possible sites. However, before any conclusive statement is possible further theoretical work is required; *e.g.* a comparative study of Ce doping of bulk BaO or BaO layers in $YBa_2Cu_3O_{7-\delta}$ and Ba doping in CeO_2 or doped CeO_2. This is, however, beyond the scope of the current work.

In Fig. 4 the obtained defect formation energies are compared to the calculated atomic crystal radius R_M (Fig. 4(a)) and the covalent radius (Fig. 4(b)).[125] Figure 4(a) shows the most stable dopants to have a crystal radius between that of $8-$coordinate Ce^{IV} and Ce^{III}, while Fig. 4(b) shows high stability for elements with a covalent radius close to that of Ce. In

both cases, the Nb dopant appears as an exception, showing a reasonably beneficial defect formation energy, while presenting a significantly lower atomic radius than the other more stable dopants. The Nb covalent radius and calculated radius R_M, however, is nicely in the range of those of the group IVb elements (Ti: 1.60Å, Zr and Hf: 1.75Å) which were shown to provide stable dopant elements.[54,55,125] The main difference between Nb and the other elements presented in this work is the fact that Nb acts as a tetravalent dopant in the $Ce_{1-x}Nb_xO_2$ system. This shows that the relation between dopant stability and radius is more complex, and that the oxidation state (in the final compound) plays an important role. As such, a higher oxidation state results in a smaller radius for stable dopant elements. In addition, it is also apparent from these figures that the order of the atomic radii differs significantly depending on the definition used. Consequently, simple stability rules based on ratios of atomic radii, for example used in the study of fluorite-pyrochlore transitions, should be treated with considerable caution since they appear to be ill-defined.[43,130]

Based on these results some extrapolations can be made regarding other dopant elements. Let us assume that the trend observed for the defect formation energies of group IVa and IVb dopants also hold for other groups.[55] Then, from the defect formation energies for Mg and Ba, we can conclude that all other group IIa elements (Be, Ca, Sr, and Ra) should segregate when used as dopant in CeO_2 making the latter well suited as support for the alkaline earth metals and their oxides.

Based on the values calculated for V and Nb, the value for Ta is expected to be below the oxygen vacancy formation energy. This indicates that Ta should be a good candidate for bulk doping of CeO_2. This is supported by the experimental work of Zhao and Gorte, who studied the influence of Ta_2O_5 doping of CeO_2 on its catalytic activity for *n*-butane.

Turning our attention to the first row *d*-block elements, the high defect formation energy for Co, Cu and Zn, and their comparable radii leads us to expect similar segregation behavior for Ni and Fe doping. On the other hand, the promising defect formation energies for La, Sm and Gd are an indication that (especially the first half of) the lanthanides are good candidates for bulk doping of CeO_2.

3.3 Bulk modulus (BM) and thermal expansion coefficients (TECs)

The modification of the elastic properties of CeO_2 due to aliovalent doping is investigated through the BM and linear TEC α. To reduce the computational cost, the BM and TEC are only calculated for dopant concentrations of 25%. Table 4 shows the BM and the linear TEC at 500 K. The BM and TEC for pure CeO_2 are given as reference. These show the LDA based value for the TEC at 300 K to be in excellent agreement
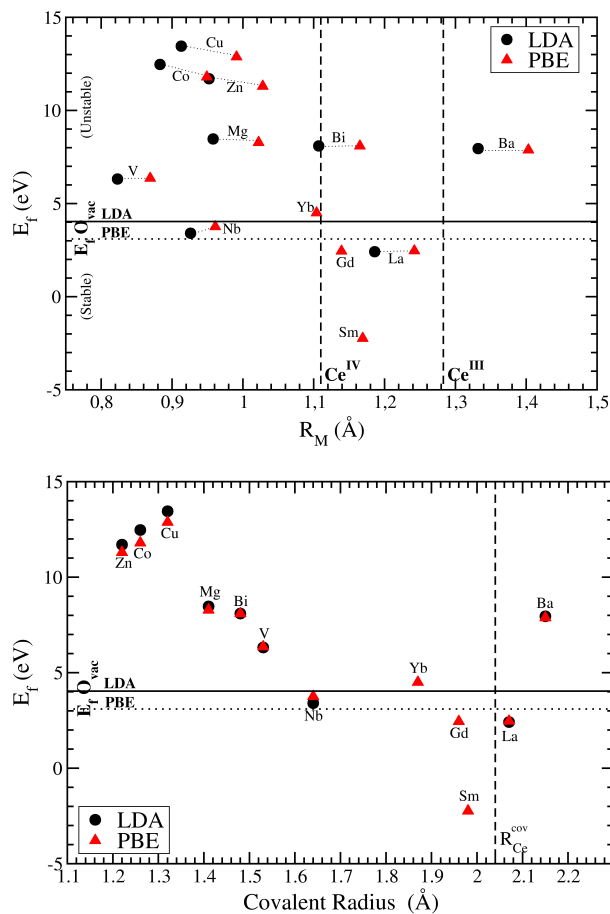
Fig. 4 The calculated formation energy E_f, for $Ce_{1-x}M_xO_2$ with $x = 0.03125$, as function of the calculated atomic radius R_M (top) and the covalent radius (bottom). [125] Top: Vertical dashed lines indicate the Shannon crystal radii for 8−coordinate Ce^{III} and Ce^{IV}. [78,79] Bottom: Vertical dashed line indicates the covalent radius for Ce R_{Ce}^{cov}. [125] Top+Bottom: The O vacancy formation energy at a vacancy concentration of 1.5% is indicated with a solid (LDA) or dotted (PBE) line.

Table 4 Bulk moduli and thermal expansion coefficients for aliovalent dopants[a]

	ox.	B_0 (Mbar)		α $(10^{-6}$ K$^{-1})$	
		LDA	PBE[b]	LDA	PBE
CeO_2		2.017	1.715	11.218	12.955
Mg	II	1.644	1.389	14.693	16.867
V	IV	2.132	1.796	11.510	13.601
Co	II	1.867	1.542	13.779	16.567
Cu	I	1.704	1.374	16.186	19.902
Zn	II	1.712	1.410	14.968	17.656
Nb	IV	2.187	1.871	10.621	12.226
Ba	II	1.580	1.321	13.544	15.608
La	III	1.835	1.556	11.809	13.618
Sm	III	−	1.595	−	13.678
Gd	III	−	1.588	−	13.744
Yb	III	−	1.534	−	15.229
Bi	III	1.874	1.575	12.631	14.836

[a] Calculated BM B_0 for CeO_2 at a dopant concentration of 25%, for LDA and PBE calculations. The linear TEC α at the same dopant concentration and a temperature of 500 K. [86] A best guess for the oxidation state (ox.) of the dopants is given. [123]
[b] In the work of Lejaeghere *et al.* [115] general error bars for PBE derived materials properties were calculated based on pure materials (single atomic species, excluding lanthanides and actinides). Assuming these error bars can be transferred to Lanthanide based oxides, the error bar on B_0 would be 0.15 Mbar.

with the experimental value ($(11.0 \pm 0.5) \times 10^{-6}$ K^{-1} at room temperature (RT), and $(11.5 \pm 0.5) \times 10^{-6}$ K^{-1} at 500 °C), while the PBE value is clearly an over-estimation. [23] With regard to the BM it is again the LDA value that shows best agreement with experiment where values in the range of 2.04–2.36 MBar have been measured. [104–106] The PBE value shows a significant underestimation, in line with the overestimation of the TEC. Of all dopants investigated in this work, only V and Nb give rise to an increase in the BM, all other dopants reduce the BM to varying degree. Comparing the BM for (the tetravalent) V and Nb dopants to those found for group IVb dopants shows them to present similar values. [54,55] For Cu, the BM was also calculated for $Ce_{0.875}Cu_{0.125}O_2$, and found to be 1.867 and 1.553 Mbar for LDA and PBE, respectively. This is within 0.01 Mbar of the average of the BM for pure CeO_2 and $Ce_{0.75}Cu_{0.25}O_2$, showing that a linear relation between the BM and dopant concentration is a reasonable assumption for $Ce_{1-x}M_xO_2$ systems.

With the exception of Nb, all investigated dopants result in an increase of the TEC. The data in Table 4 reveal that low dopant valence leads to a large increase in the TEC and high valence leads to a small increase and even decrease of the TEC.

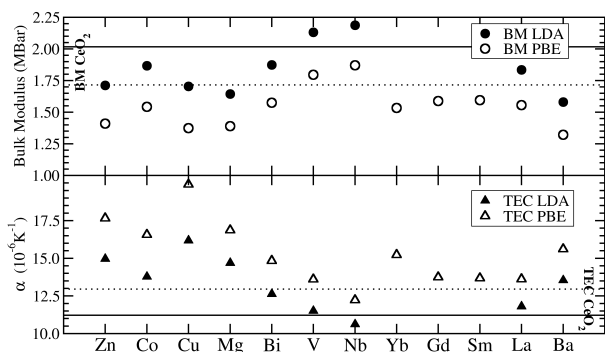Comparison of the BM and the TEC in Fig. 5 shows clearly

Fig. 5 Calculated BM and linear TEC α at 500 K for $Ce_{0.75}M_{0.25}O_2$. Calculated values (LDA: solid line, PBE: dotted line) for pure CeO_2 are given for reference. The elements are sorted with regard to increasing Covalent radius.[125]

Fig. 6 Calculated linear TEC α for different dopants based on (a) LDA and (b) PBE total energies and volumes. The calculated TEC of CeO_2 (black solid curve) is given as reference.

opposite trends of the BM and TEC, as was also observed for group IV elements, again showing the expected inverse correlation between the BM and the TEC.[55,131,132] Only vanadium shows a slightly different behavior with both the TEC and BM being larger than the CeO_2 values. Close investigation of the vanadium TEC in Fig. 6a shows that the vanadium curve crosses the TEC curve for pure CeO_2 at around 250 K, so below this temperature the inverse behavior of the TEC and BM is restored.

Figure 6a also shows the TEC for two different Cu dopant concentrations. From RT up to at least 1000 K a nearly linear influence of the dopant concentration on the TEC change is observed, indicating that for aliovalently doped systems in highly oxidizing atmosphere the TEC may also be linearly interpolated. This linear behavior supports the inherent assumption underlying the experimental practice of codoping in several ceria based applications.[68,133]

Figure 6b shows the TEC of the lanthanides La, Sm, and Gd to coincide nicely, while the Yb curve shows much higher values. This difference in behavior is most likely linked to the filled $4f$ shell of Yb (which is only partially filled for Sm and Gd). Further investigation of lanthanide doped systems is required to have the full picture of the mechanism at work. Similar as was found for group IV doped systems, this behavior shows the importance of filled shells near the Fermi-level.

Several authors have noted that one should be very careful when comparing calculated and experimentally obtained lattice parameters for CeO_2, since the former are generally calculated at zero Kelvin, while the latter are measured at RT. These authors suggest to linearly extrapolate the calculated lattice parameter making use of the '*linear TEC*'. In this setup the coefficient is assumed to be a constant, and often taken from experiment. As is shown in Fig. 6, the linear TEC shows quite a non-linear behavior at low temperature.[134] Taking this
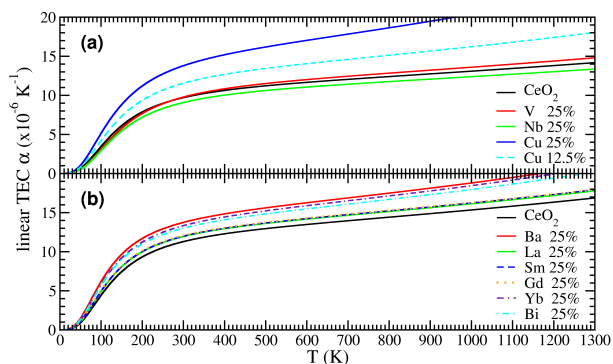
behavior into account one can obtain a more accurate value of the lattice parameter at RT. Zero Kelvin and RT values of the lattice parameter of doped CeO_2 are shown in Table 2. The thermal contribution to the lattice parameter at RT is fairly limited and is of the order of 0.02–0.04 Å, for dopant concentrations of 25%. Because this can be comparable to the variation of the lattice parameter due to doping, this can result in differently doped systems having the same lattice parameter at elevated temperatures (e.g. Sm and Bi doped (25%) CeO_2 at about 1065 K, and pure and Yb doped (25%) CeO_2 at about 1024 K). As a result, codoped systems or interfaces between layers of differently doped CeO_2 may experience reduced strain at elevated temperatures. The opposite is to be expected as well, and increased segregation or interface strain at elevated temperatures could be a consequence. This latter aspect is of importance when perfect interfaces are required, and should be considered when crack formation in thin films is an issue.[16,17,19,21]

4 Inclusion of Vacancies

Since the configuration of dopants and oxygen vacancies for the systems studied is essentially unknown, different configurations need to be investigated. However, since it is neither our goal nor our intent to find the exact ground state configuration of these systems, but rather to investigate the influence of vacancies, we restrict ourselves to a subset of dopant elements and a small set of configurations for the different dopants. A full study of the configurational space is beyond the scope of this study. The subset of dopant elements consists of Cu^I, Zn^{II}, and Gd^{III}. In addition, vacancies in pure CeO_2 are added as reference.

The different vacancy geometries are described in Sec. 2 and the notation 'NV' is used to indicate the 'No Vacancy' reference systems, *i.e.* $Ce_{1-x}M_xO_2$ with M=Cu, Zn, or Gd.

All systems presented, contain 1 oxygen vacancy per dopant atom, resulting in charge under-compensation (Cu), compensation (Zn), and over-compensation (Gd).[56] For these systems the vacancy formation energy E_{vac} is calculated as:

$$E_{vac} = E_{Ce_{1-x}M_xO_{2-y}} + \frac{N_{vac}}{2}E_{O_2} - E_{Ce_{1-x}M_xO_2}, \qquad (4)$$

with N_{vac} the number of oxygen vacancies,[135] E_{O_2} the total energy of an oxygen molecule, and $E_{Ce_{1-x}M_xO_{2-y}}$ and $E_{Ce_{1-x}M_xO_2}$ the total energies of the system with and without vacancies, respectively.

4.1 Oxygen and cerium vacancies in CeO$_2$

Before investigating the combined influence of dopants and vacancies, the influence of oxygen and cerium vacancies on pure CeO$_2$ is briefly discussed. Table 5 shows the vacancy formation energy of both Ce and O vacancies, which are in good agreement with the vacancy formation energies calculated by Keating et al.[136] From this, it is clear that Ce vacancies are highly unfavorable, in agreement with experimental observations.[2,23] In addition, the relatively small change of the lattice parameter appears to be strongly functional dependent.

The vacancy formation energy of the oxygen vacancies on the other hand shows a significant concentration dependence (in contrast to the calculations for the doped systems of the previous section). In addition, the calculated lattice expansion is clearly non-linear, with a similar trend for LDA and PBE calculations. The expansion of the lattice parameter due to the presence of oxygen vacancies is experimentally known, and theoretically understood as a consequence of the transition from Ce^{IV} to Ce^{III} of two Ce atoms neighboring the oxygen vacancy. Since the atomic crystal radius of Ce^{III} is significantly larger than Ce^{IV} (1.283Å instead of 1.11Å) the lattice will expand.[2,23,78,79] The non-linearity shown here, indicates that for aliovalent dopants charge compensating vacancies may give rise to non-Vegard law behavior, due to Ce$^{IV} \longrightarrow$ Ce^{III} transitions.

Interesting to note is the large impact of the vacancies on the BM and TEC of CeO$_2$. Figure 7a shows a dramatic increase in the linear TEC due to the presence of vacancies. It is clear that the inverse relation between the BM and the TEC is retained for vacancies.

4.2 Aliovalent dopants Cu, Zn and Gd combined with a single oxygen vacancy

4.2.1 Vacancy formation energy. If one assumes the oxidation states of Cu, Zn and Gd as dopants for CeO$_2$ to be I, II, and III, respectively, then the introduction of a single oxygen vacancy for every dopant ion will result in undercompensation in case of Cu, nominal charge compensation
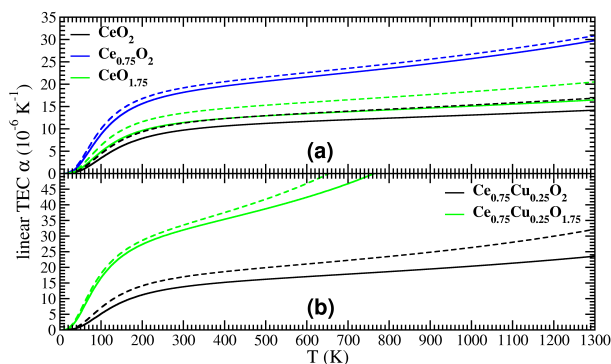

Fig. 7 Calculated linear TEC α for different systems containing vacancies. (a) Comparison of the influence of oxygen and cerium vacancies, (b) Cu doping with and without oxygen vacancies. LDA results are shown as solid lines and PBE as dashed lines.

for Zn, and over-compensation in case of Gd.[123] Table 6 shows the vacancy formation energies for these three dopant elements. For all systems, the absolute value of E_{vac} is of the order of 1 eV. Because the formation energy of a doped system including oxygen vacancies can be written as $E_{f,vac} = E_f + E_{vac}$, where E_f is the formation energy of the NV system, the introduction of an oxygen vacancy in a Cu or Zn doped system will result in an improved stability. However, since $E_{f,vac}$ is positive this means that the formation of oxygen vacancies will not prevent phase segregation and promote the formation of bulk doped CeO$_2$. This would require E_{vac} to be more negative than E_f is positive.

In contrast, the Gd doped system appears to destabilize due to the introduced oxygen vacancy. This destabilization is merely a consequence of the fact that the vacancy concentration is higher than the nominal concentration required for charge compensation. Table 7 shows the vacancy formation energies for different configurations containing two Gd dopant ions and a single vacancy leading to exact charge compensation. In this situation, the vacancies also have a stabilizing effect on the Gd doped system. Note that the different configurations without vacancies are nearly degenerate; all have defect formation energies within a range of 50 meV. The oxygen vacancy formation energies on the other hand are spread over a wider range, and show a correlation with the chemical environment defined as the surrounding cation tetrahedron (cf. Fig. 1a). The oxygen vacancy appears to prefer multiple dopant cations in the tetrahedral surrounding in case of Gd doping. Based on the A and B configurations, there appears to be an improvement of the vacancy formation energy of 150 meV per Gd cation included in the tetrahedron. This shows good agreement with the association energy of 0.13 eV for the Gd-oxygen vacancy complex.[5] It is also in line with earlier atomistic calculations of Catlow and collaborators, and

Table 5 Properties of vacancies in non-doped $CeO_2{}^a$

		E_{vac} (eV)				Δa_0 (%)				B_0 (Mbar)	α (10^{-6} K^{-1})
Vac. conc. (%)		12.5%	6.25%	1.852%	1.563%	12.5%	6.25%	1.852%	1.563%	12.5%	12.5%
O Vac.	LDA	5.006	4.440	4.054	4.035	0.775	0.510	0.176	0.141	1.568	12.912
	PBE	4.145	3.476	3.075	3.097	0.908	0.606	0.193	0.165	1.320	15.287
Vac. conc. (%)		25%	12.5%	3.704%	3.125%	25%	12.5%	3.704%	3.125%	25%	25%
Ce Vac.	LDA	17.549	17.779	17.857	17.829	−0.270	−0.032	−0.016	−0.028	1.023	20.650
	PBE	16.255	16.543	16.611	16.592	0.560	0.266	0.063	0.061	0.858	21.609

^{a} Properties of vacancies in non-doped CeO_2: vacancy formation energy E_{vac} as given in Eq. (4), lattice expansion Δa_0, bulk modulus B_0 and linear thermal expansion coefficient α. Vacancy concentrations are indicated and the linear thermal expansion coefficient value α is given for a temperature of 500 K.

Table 6 Properties for Cu, Zn and Gd doped CeO_2 containing oxygen vacancies^a

	E_{vac} (eV)			B_0 (Mbar)			ΔV (%)			Δa_0 (%)		
	Cu	Zn	Gd	Cu	Zn	Gd	Cu	Zn	Gd	Cu	Zn	Gd
c111 NV	12.922^b	11.057^b	2.396^b	1.37	1.41	1.59	−4.124	−3.189	0.274	−1.394	−1.074	0.091
c111 V$_B$	−0.800	−0.882	1.929	0.87	0.38	0.86	−0.568	−1.529	1.563	−0.190	−0.512	0.518
p222 NV	12.878^b	11.249^b	2.445^b	1.55	–	–	−2.145	−1.529	0.158	−0.733	−0.526	0.039
p222 V$_A$	−0.048	−0.604	1.395	1.01	1.03	1.00	0.619	0.552	1.371	0.193	0.170	0.442
p222 V$_B$	−0.422	−1.200	1.364	1.04	1.09	1.31	−1.173	−1.416	1.116	−0.406	−0.488	0.357

^{a} Calculated vacancy formation energy (E_{vac}) as given by Eq. (4), bulk modulus (B_0), and change in volume (ΔV) and lattice expansion (Δa_0) for Cu, Zn, and Gd doped CeO_2 including a single vacancy per supercell. ΔV and Δa_0 are taken with regard to pure CeO_2. All calculations are performed using PBE functionals. Vacancy concentrations are 12.5 (c111) and 6.25% (p222). The different configurations are shown in Fig. 1. NV indicates the reference systems without vacancies.
^{b} For the systems without vacancies, the formation energy E_f is repeated. Note that the formation energy of a doped system with oxygen vacancies $E_{f,vac} = E_f + E_{vac}$.

supports the predicted instability of a pyrochlore phase for $Ce_2Gd_2O_7$ by Minervini and collaborators.[43,137,138] For La, which is also a trivalent dopant for CeO_2, an opposite trend was noted for the 50% doped system.[38] Also for Cu and Zn dopants, beneficial behavior is observed when dopant cations are present in the tetrahedron surrounding the vacancy, although in these cases the effect is more pronounced. In addition, comparison of the vacancy formation energies at different dopant concentrations shows that the dopant concentration (annex vacancy concentration) has a strong influence on E_{vac}. For Cu doping an increase in E_{vac} with the dopant concentration is shown, while a decrease is seen for both Zn and Gd. The origin of this different behavior may be either due to the dopant species or the fact that the Cu system contains a too low vacancy concentration per dopant. In the latter case, increasing the Cu concentration also increases the system vacancy concentration. As a result, single oxygen vacancies may interact with different Cu ions, presenting a higher apparent oxygen vacancy concentration for the Cu ions. This reduces the effective vacancy deficiency increasing E_{vac}. The same inter-

Table 7 Oxygen vacancy formation energies for several $Ce_{0.75}Gd_{0.25}O_{1.875}$ configurations^a

	E_{vac} (eV)				$\Delta V (\%)^c$
	NV^b	V$_A$	V$_B$	V$_C$	V$_B$
# Gd	na	0	1	2	1
A	2.380	−0.137	−0.273	−0.440	0.943
B	2.365	−0.037	–	−0.310	–
C	2.398	–	−0.392	–	0.871
D	2.402	–	−0.402	–	0.866

^{a} Oxygen vacancy formation energies for different $Ce_{0.75}Gd_{0.25}O_{1.875}$ configurations. NV indicates configurations without oxygen vacancies. The different configurations are shown in Fig. 2. The number of Gd ions in the tetrahedron surrounding the vacancy is given.
^{b} For the systems without vacancies, the formation energy E_f is presented. Note that the formation energy of a doped system with oxygen vacancies $E_{f,vac} = E_f + E_{vac}$.
^{c} Change of the volume relative to the NV configuration.

action between the vacancies and the dopant elements would, in the case of Zn, result in an apparent over-compensation, or, in the case of Gd, even further increase the already present over-compensation.

It is clear that aliovalent dopants induce additional oxygen vacancies in CeO_2 resulting in a stabilization of the structure. The formation of oxygen vacancies is, however, limited by the number of dopants and their oxidation state, supporting the concept of charge compensating vacancies. The formation of dopant-vacancy complexes in case of Cu and Gd may reduce some of the strain due to the undercoordinated nature of these dopants (*cf.* Fig. 3 and sec. 3.1). In addition, the formation of such complexes may lead to small dopant-oxide clusters in the CeO_2 crystals or at their boundaries, masking the dopant segregation in experiment. X-ray diffraction investigations searching for signatures of the pure metals will, in such case, reveal (accurately) that no metal clusters are present,[30] despite the segregation of the dopant atoms from the CeO_2 bulk.

4.2.2   Crystal structure. Where the introduction of a homogeneous distribution of dopants mainly results in an isotropic lattice expansion, the addition of charge compensating oxygen vacancies also results in an increase of the angles between the lattice vectors. Although these changes tend to be quite small ($< 5°$ in $Ce_{0.75}Cu_{0.25}O_{1.75}$, and $< 0.5°$ in $Ce_{0.75}Gd_{0.25}O_{1.75}$), they are often anisotropic. As a result we define the change in the lattice parameter for doped systems containing oxygen vacancies as:

$$\Delta a_0 = \frac{(\sqrt[3]{V} - a_{CeO_2})}{a_{CeO_2}} \cdot 100\% \qquad (5)$$

with a_{CeO_2} the lattice parameter of pure CeO_2 and V the volume per formula unit of the doped system. Table 6 shows both the change in the volume and lattice parameter for the Cu, Zn, and Gd doped systems. In each case, the oxygen vacancies result in an expansion of the volume (lattice parameter) compared to the system without vacancies, either compensating the lattice compression (Cu and Zn) or further increasing the lattice expansion.

In experiments, Bera *et al.* observe only a very small lattice contraction of -0.01% for a system with 5% Cu doping.[24] This is much smaller than the value presented in Table 6, but this can easily be understood. Firstly, the Cu doped systems presented here, contain much higher Cu concentrations (25 and 12.5%) than the system of Bera *et al.*, and secondly, the oxygen vacancy concentration in the system of Bera *et al.* contains a much higher relative oxygen vacancy concentration than in the presented systems. As a result, the lattice contraction theoretically presented in Table 6 would be even further compensated if a higher vacancy concentration was used, indicating that values of the order presented by Bera *et al.* are

reasonable (and even small expansions should be considered possible).

In case of Gd doping without oxygen vacancies, we found the lattice expansion to be very small (slope of 0.015 for its Vegard law in Table 2). However, Table 7 shows the lattice will expand further due to the presence of oxygen vacancies (volume increase of $+0.9\%$ for $Ce_{0.75}Gd_{0.25}O_{1.875}$ compared to $Ce_{0.75}Gd_{0.25}O_2$). Taking this additional expansion into account the Vegard law slope increases to 0.0804 in perfect agreement with the experimentally measured slope of 0.0813 for Gd doped CeO_2.[122]

In addition, comparison of ΔV for $Ce_{0.75}Gd_{0.25}O_{1.75}$ in Table 6 ($+1.563\%$) to the values for $Ce_{0.75}Gd_{0.25}O_{1.875}$ in Table 7 ($+0.9\%$) shows a clear dependence on the vacancy concentration. As a result, doped CeO_2 compounds should be expected to show breathing behavior under varying oxidizing atmosphere, such as for example car exhaust catalysts.

As would be expected from the vacancy induced $Ce^{IV} \longrightarrow Ce^{III}$ transition, Table 6 also shows the volume (lattice parameter) to increase with the number of Ce atoms in the tetrahedral surrounding. This is also in line with earlier results obtained for $Ce_{0.5}La_{0.5}O_{1.75}$.[38]

4.2.3   Bulk modulus. In Sec. 4.1 it was shown that the introduction of vacancies has a strong influence on the CeO_2 BM. Unlike the volume and lattice parameter change, dopants and the oxygen vacancies have a compound effect on the BM (and TEC), as is seen in Table 6. However, it is interesting to note that the chemical environment of the vacancy has only limited influence on the BM (compare the V_A and V_B values of the p222 supercell), when no charge over-compensation is present. Figure 7b shows that the decrease of the BM goes hand in hand with the increase of the TEC as was observed for systems without vacancies, showing this behavior to be a universal trend.

5   Conclusion

In summary, we have studied the structural and mechanical properties of fluorite CeO_2 doped with several aliovalent dopants using *ab-initio* DFT calculations. Dopant concentrations in the range of $0 \leq x \leq 25$ % are investigated, and for Cu, Zn, and Gd dopants also the influence of additional oxygen vacancies is studied.

We have shown that for fluorite CeO_2 doped with aliovalent dopants the lattice expansion shows Vegard law behavior under oxidizing atmosphere. In addition, the Shannon crystal radius of the dopant element can be calculated in a simple way from the lattice parameter. The calculated atomic radii indicated a preference for a lowered coordination for (most) aliovalent dopants. This preference is expected to be a driving force for local lattice reconstructions at dopant sites. The

introduction of charge compensating oxygen vacancies results in an increase of the lattice parameter, which (partially) compensates the lattice contraction observed for small dopants.

As was previously found for group IV dopants, aliovalent dopants also show an inverse relation between the change in bulk modulus and thermal expansion coefficient.[55] Different dopant elements give rise to different changes in the bulk moduli and thermal expansion coefficients, however, the introduction of oxygen vacancies has a much larger effect, and decreases the bulk modulus significantly.

Defect formation energies are calculated and compared to the oxygen vacancy formation energy to indicate the preference for bulk doping over segregation of the dopant ions. For the systems investigated we conclude that bulk (substitutional) doping is very unfavorable for Cu, Co, and Zn, while La, Gd, and Sm present themselves as very favorable bulk dopants. No clear relation between the defect formation energy and either the covalent or calculated crystal radius appears to exist.

Vacancy formation energies are calculated for different configurations containing 25 and 12.5% Cu, Zn or Gd. For systems where the oxygen vacancies over compensate the charge deficiency due to the aliovalent dopant, the oxygen vacancies are found to be unstable, while being stable otherwise. The strong dependence of the oxygen vacancy formation energy on the chemical environment is indicative for the formation of metal-vacancy complexes for many aliovalent dopants. Clustering of such complexes, essentially leading to dopant-oxide clusters in CeO_2 may effectively hide dopant segregation in experiments. Although oxygen vacancies are found to stabilize the systems, their contribution remains too small to make bulk doping favorable for Cu, Co and Zn.

6 Acknowledgement

Notes and references

1 H. L. Tuller and A. S. Nowick, *J. Electrochem. Soc.*, 1975, **122**, 255–259.

2 A. Trovarelli, *Catal. Rev.-Sci. Eng.*, 1996, **38**, 439–520.

3 M. Manzoli, G. Avgouropoulos, T. Tabakova, J. Papavasiliou, T. Ioannides and F. Boccuzzi, *Catal. Today*, 2008, **138**, 239 – 243.

4 J. Kašpar, P. Fornasiero and M. Graziani, *Catal. Today*, 1999, **50**, 285–298.

5 B. Steele, *Solid State Ionics*, 2000, **129**, 95–110.

6 Z. Shao and S. M. Haile, *Nature*, 2004, **431**, 170–173.

7 Z. Yang, G. Luo, Z. Lu and K. Hermansson, *J. Chem. Phys.*, 2007, **127**, 074704.

8 V. Shapovalov and H. Metiu, *J. Catal.*, 2007, **245**, 205–214.

9 A. D. Mayernick and M. J. Janik, *J. Phys. Chem. C*, 2008, **112**, 14955–14964.

10 T. Désaunay, A. Ringuedé, M. Cassir, F. Labat and C. Adamo, *Surf. Sci.*, 2012, **606**, 305–311.

11 H. Yao and Y. Yu Yao, *J. Catal.*, 1984, **86**, 254–265.

12 Q. Fu, H. Saltsburg and M. Flytzani-Stephanopoulos, *Science*, 2003, **301**, 935–938.

13 J. R. McBride, K. C. Hass, B. D. Poindexter and W. H. Weber, *J. Appl. Phys.*, 1994, **76**, 2435–2441.

14 X. Cao, R. Vassen, W. Fischer, F. Tietz, W. Jungen and D. Stover, *Adv. Mater.*, 2003, **15**, 1438–1442.

15 X. Q. Cao, R. Vassen and D. Stoever, *J. Eur. Ceram. Soc.*, 2004, **24**, 1–10.

16 M. Paranthaman, A. Goyal, F. List, E. Specht, D. Lee, P. Martin, Q. He, D. Christen, D. Norton, J. Budai and D. Kroeger, *Physica C*, 1997, **275**, 266 – 272.

17 S. Oh, J. Yoo, K. Lee, J. Kim and D. Youm, *Physica C*, 1998, **308**, 91 – 98.

18 G. Penneman, I. Van Driessche, E. Bruneel and S. Hoste, Euro Ceramics VIII, Pts 1-3, 2004, pp. 501–504.

19 Y. Takahashi, Y. Aoki, T. Hasegawa, T. Maeda, T. Honjo, Y. Yamada and Y. Shiohara, *Physica C*, 2004, **412-414, Part 2**, 905–909.

20 K. Knoth, B. Schlobach, R. Hühne, L. Schultz and B. Holzapfel, *Physica C*, 2005, **426-431, Part 2**, 979–984.

21 N. Van de Velde, D. Van de Vyver, O. Brunkahl, S. Hoste, E. Bruneel and I. Van Driessche, *Eur. J. Inor. Chem.*, 2010, **2010**, 233–241.

22 V. Narayanan, P. Lommens, K. De Buysser, D. E. P. Vanpoucke, R. Huehne, L. Molina, G. Van Tendeloo, P. Van Der Voort and I. Van Driessche, *J. Mater. Chem.*, 2012, **22**, 8476–8483.

23 M. Mogensen, N. M. Sammes and G. A. Tompsett, *Solid State Ionics*, 2000, **129**, 63–94.

24 P. Bera, K. R. Priolkar, P. R. Sarode, M. S. Hegde, S. Emura, R. Kumashiro and N. P. Lalla, *Chem. Mater.*, 2002, **14**, 3591–3601.

25 B. Li, X. Wei and W. Pan, *J. Power Sources*, 2008, **183**, 498–505.

26 D. Mullins, P. Radulovic and S. Overbury, *Surf. Sci.*, 1999, **429**, 186–198.

27 H. C. Aspinall, J. Bacsa, A. C. Jones, J. S. Wrench, K. Black, P. R. Chalker, P. J. King, P. Marshall, M. Werner, H. O. Davies and R. Odedra, *Inorg. Chem.*, 2011, **50**, 11644–11652.

28 S. Rossignol, F. Gerard and D. Duprez, *J. Mater. Chem.*, 1999, **9**, 1615–1620.

29 I. Van Driessche, G. Penneman, C. De Meyer, I. Stambolova, E. Bruneel and S. Hoste, Euro Ceramics VII, PT 1-3, Brandrain 6, CH-8707 Zurich-Uetikon, Switzerland, 2002, pp. 479–482.

30 B. Ali, L. R. Shah, C. Ni, J. Q. Xiao and S. I. Shah, *J. Phys.: Condens. Matter*, 2009, **21**, 456005.

31 L. Claparede, N. Clavier, N. Dacheux, P. Moisy, R. Podor and J. Ravaux, *Inor. Chem.*, 2011, **50**, 9059–9072.

32 D. Horlait, N. Clavier, S. Szenknect, N. Dacheux and V. Dubois, *Inor. Chem.*, 2012, **51**, 3868–3878.

33 Y. Q. Song, H. W. Zhang, Q. H. Yang, Y. L. Liu, Y. X. Li, L. R. Shah, H. Zhu and J. Q. Xiao, *J. Phys.: Condens. Matter*, 2009, **21**, 125504.

34 M. Yashima, *J. Phys. Chem. C*, 2009, **113**, 12658–12662.

35 Z. Yang, Y. Wei, Z. Fu, Z. Lu and K. Hermansson, *Surf. Sci.*, 2008, **602**, 1199–1206.

36 D. A. Andersson, S. I. Simak, N. V. Skorodumova, I. A. Abrikosov and B. Johansson, *PNAS*, 2006, **103**, 3518–3521.

37 Z. Lu, Z. Yang, B. He, C. Castleton and K. Hermansson, *Chem. Phys. Lett.*, 2011, **510**, 60–66.

38 D. E. P. Vanpoucke, P. Bultinck, S. Cottenier, V. Van Speybroeck and I. Van Driessche, *Phys. Rev. B*, 2011, **84**, 054110.

39 P. P. Dholabhai, J. B. Adams, P. A. Crozier and R. Sharma, *J. Mater. Chem.*, 2011, **21**, 18991–18997.

40 O. Hellman, N. V. Skorodumova and S. I. Simak, *Phys. Rev. Lett.*, 2012, **108**, 135504.

41 M. J. D. Rushton, A. Chroneos, S. J. Skinner, J. A. Kilner and R. W. Grimes, *Sol. State Ion.*, 2013, **230**, 37–42.

42 P. R. L. Keating, D. O. Scanlon and G. W. Watson, *J. Mater. Chem. C*, 2013, **1**, 1093–1098.

43 L. Minervini, R. W. Grimes and K. E. Sickafus, *J. Am. Ceram. Soc.*, 2000, **83**, 1873–1878.

44 F. Ye, T. Mori, D. R. Ou and A. N. Cormack, *Solid State Ionics*, 2009, **180**, 1127 – 1132.

45 X. Wei, W. Pan, L. Cheng and B. Li, *Solid State Ionics*, 2009, **180**, 13–17.

46 M. Alaydrus, M. Sakaue, S. M. Aspera, T. D. K. Wungu, T. P. T. Linh, H. Kasai, T. Ishihara and T. Mohri, *J. Phys.: Condens. Matter*, 2013, **25**, 225401.

47 K. M. Ryan, J. P. McGrath, R. A. Farrell, W. M. O'Neill, C. J. Barnes and M. A. Morris, *J. Phys. Condens. Matter*, 2003, **15**, L49–L58.

48 F. W. Bezerra Lopes, C. P. de Souza, A. M. Vieira de Morais, J.-P. Dallas and J.-R. Gavarri, *Hydrometallurgy*, 2009, **97**, 167–172.

49 M. Reddy, Benjaram, L. Katta and G. Thrimurthulu, *Chem. Mater.*, 2010, **22**, 467–475.

50 D. Horlait, L. Claparède, N. Clavier, S. Szenknect, N. Dacheux, J. Ravaux and R. Podor, *Inor. Chem.*, 2011, **50**, 7150–7161.

51 D. A. Andersson, S. I. Simak, N. V. Skorodumova, I. A. Abrikosov and B. Johansson, *Phys. Rev. B*, 2007, **76**, 174119.

52 D. A. Andersson, S. I. Simak, N. V. Skorodumova, I. A. Abrikosov and B. Johansson, *Appl. Phys. Lett.*, 2007, **90**, 031909.

53 Y. Tang, H. Zhang, L. Cui, C. Ouyang, S. Shi, W. Tang, H. Li, J.-S. Lee and L. Chen, *Phys. Rev. B*, 2010, **82**, 125104.

54 D. E. P. Vanpoucke, S. Cottenier, V. Van Speybroeck, P. Bultinck and I. Van Driessche, *Appl. Surf. Sci.*, 2012, **260**, 32–35.

55 D. E. P. Vanpoucke, S. Cottenier, V. Van Speybroeck, I. Van Driessche and P. Bultinck, *J. Am. Ceram. Soc.*, 2014, **97**, 258–266.

56 It is at this point important to note that all the systems under study in this work are charge neutral from the electronic point of view, *i.e.* there are as many positive as negative charges in each cell. As such the term "charge compensating vacancy" and reference to it by the use of terms like "charge compensation" may be considered confusing. The terminology, however, originates in the study of ionic conductivity. There, the substitution of one cation by another will, when using the Kröger-Vink notation, always indicate the change in valence at the substitution site as a charge on the substituent element. For example, if MgO is dissolved in CeO_2, tetravalent Ce is substituted by divalent Mg, which in Kröger-Vink notation can be written as: [139]

$$MgO \xrightarrow{CeO_2} Mg_{Ce}'' + O_O^{\times} + V_O^{\bullet\bullet}.$$

The right hand side shows how one CeO_2 unit is replaced by a MgO unit: The Mg at a Ce site, in which case the oxidation state of the site changes from IV to II, indicated as a double negative charge at the site; the O atom at an O site, with no change of the oxidation state; and a vacancy (V) at an oxygen site, changing the site's oxidation state from −II to 0, indicated as a double positive charge. If within such a description the vacancy is omitted, the sum of the site charges will be non-zero. For this reason the vacancy is referred to as a "charge compensating vacancy". One may remark that one is actually balancing oxidation states (or valencies, *cf.* Ref. [123]) and not charges, and as such "valence compensating vacancy" would be a better suited term. However, charge compensating vacancy is the terminology used in (experimental) literature, so we will also use it to keep this link, and to avoid confusion on this account.

57 L. Kundakovic and M. Flytzani-Stephanopoulos, *Appl. Catal. A*, 1998, **171**, 13–29.

58 L. Kundakovic and M. Flytzani-Stephanopoulos, *J. Catal.*, 1998, **179**,

203 – 221.

59 X. Wang, J. A. Rodriguez, J. C. Hanson, D. Gamarra, A. Martínez-Arias and M. Fernández-García, *J. Phys. Chem. B*, 2005, **109**, 19595–19603.

60 X. Wang, J. A. Rodriguez, J. C. Hanson, D. Gamarra, A. Martínez-Arias and M. Fernández-García, *J. Phys. Chem. B*, 2006, **110**, 428–434.

61 R. de Biasi and M. Grillo, *J. Sol. State Chem.*, 2005, **178**, 1973–1977.

62 B. Li, X. Wei and W. Pan, *Int. J. Hydrogen Energy*, 2010, **35**, 3018 – 3022.

63 M. Anwar, S. Kumar, N. Arshi, F. Ahmed, Y. Seo, C. Lee and B. H. Koo, *J. Alloys Compd.*, 2011, **509**, 4525–4529.

64 F. Brisse and O. Knop, *Can. J. Chem.*, 1967, **45**, 609–614.

65 J. S. Bae, W. K. Choo and C. H. Lee, *J. Eur. Ceram. Soc.*, 2004, **24**, 1291–1294.

66 R. de Biasi and M. Grillo, *J. Alloys Compd.*, 2008, **462**, 15–18.

67 Y. She, Q. Zheng, L. Li, Y. Zhan, C. Chen, Y. Zheng and X. Lin, *Int. J. Hydrogen Energy*, 2009, **34**, 8929–8936.

68 A. Ainirad, M. K. Motlagh and A. Maghsoudipoor, *J. Alloys Compd.*, 2011, **509**, 1505–1510.

69 A. Tiwari, V. M. Bhosle, S. Ramachandran, N. Sudhakar, J. Narayan, S. Budak and A. Gupta, *Appl. Phys. Lett.*, 2006, **88**, 142511.

70 B. Vodungbo, Y. Zheng, F. Vidal, D. Demaille, V. H. Etgens and D. H. Mosca, *Appl. Phys. Lett.*, 2007, **90**, 062510.

71 V. Fernandes, J. J. Klein, N. Mattoso, D. H. Mosca, E. Silveira, E. Ribeiro, W. H. Schreiner, J. Varalda and A. J. A. de Oliveira, *Phys. Rev. B*, 2007, **75**, 121304.

72 Y. Q. Song, H. W. Zhang, Q. Y. Wen, H. Zhu and J. Q. Xiao, *J. Appl. Phys.*, 2007, **102**, 043912.

73 Q.-Y. Wen, H.-W. Zhang, Y.-Q. Song, Q.-H. Yang, H. Zhu and J. Q. Xiao, *J. Phys.: Condens. Matter*, 2007, **19**, 246205.

74 R. K. Singhal, P. Kumari, S. Kumar, S. N. Dolia, Y. T. Xing, M. Alzamora, U. P. Deshpande, T. Shripathi and E. Saitovitch, *J. Phys. D: Appl. Phys.*, 2011, **44**, 165002.

75 J. Sacanell, M. A. Paulin, V. Ferrari, G. Garbarino and A. G. Leyva, *Appl. Phys. Lett.*, 2012, **100**, 172405.

76 D. Xu, X. Liu, S. Xu, D. Yan, L. Pei, C. Zhu, D. Wang and W. Su, *Solid State Ionics*, 2011, **192**, 510–514.

77 H.-C. Yao, X.-L. Zhao, X. Chen, J.-C. Wang, Q.-Q. Ge, J.-S. Wang and Z.-J. Li, *J. Power Sources*, 2012, **205**, 180–187.

78 J. D. Van Horn, *Electronic Table of Shannon Ionic Radii*, 2001, http://v.web.umkc.edu/vanhornj/shannonradii.htm downloaded 08/13/2010.

79 R. D. Shannon, *Acta Cryst.*, 1976, **A32**, 751–767.

80 P. E. Blöchl, *Phys. Rev. B*, 1994, **50**, 17953–17979.

81 G. Kresse and D. Joubert, *Phys. Rev. B*, 1999, **59**, 1758–1775.

82 D. M. Ceperley and B. J. Alder, *Phys. Rev. Lett.*, 1980, **45**, 566–569.

83 J. P. Perdew, K. Burke and M. Ernzerhof, *Phys. Rev. Lett.*, 1996, **77**, 3865–3868.

84 G. Kresse and J. Hafner, *Phys. Rev. B*, 1993, **47**, 558–561.

85 G. Kresse and J. Furthmüller, *Phys. Rev. B*, 1996, **54**, 11169–11186.

86 LDA values for Sm, Gd, and Yb are missing since no LDA PAW potentials are available in the used distribution of the VASP program.

87 S. Rossignol, F. Gerard, D. Mesnard, C. Kappenstein and D. Duprez, *J. Mater. Chem.*, 2003, **13**, 3017–3020.

88 A. A. Maradudin, E. W. Montroll, G. H. Weiss and I. P. Ipatova, *Theory of lattice dynamics in the harmonic approximation*, Academic press, New York, 2nd edn, 1971.

89 M. A. Blanco, A. M. Pendas, E. Francisco, J. M. Recio and R. Franco, *Theochem-J. Mol. Struct.*, 1996, **368**, 245–255.

90 E. Francisco, M. A. Blanco and G. Sanjurjo, *Phys. Rev. B*, 2001, **63**, 094107.

91 D. E. P. Vanpoucke, *HIVE v2.1*, 2011, http://users.ugent.be/~devpouck/hive_refman/index.html.

92 F. D. Murnaghan, *Proc. Natl. Acad. Sci. USA*, 1944, **30**, 244–247.

93 F. Birch, *Phys. Rev.*, 1947, **71**, 809–824.

94 S. Fabris, S. de Gironcoli, S. Baroni, G. Vicario and G. Balducci, *Phys. Rev. B*, 2005, **71**, 041102.

95 C. W. M. Castleton, J. Kullgren and K. Hermansson, *J. Chem. Phys.*, 2007, **127**, 244704.

96 D. A. Andersson, S. I. Simak, B. Johansson, I. A. Abrikosov and N. V. Skorodumova, *Phys. Rev. B*, 2007, **75**, 035109.

97 C. Loschen, J. Carrasco, K. M. Neyman and F. Illas, *Phys. Rev. B*, 2007, **75**, 035115.

98 J. J. Plata, A. M. Márquez and J. F. Sanz, *J. Chem. Phys.*, 2012, **136**, 041101.

99 D. E. P. Vanpoucke, *PhD thesis*, Ghent, 2012.

100 N. V. Skorodumova, R. Ahuja, S. I. Simak, I. A. Abrikosov, B. Johansson and B. I. Lundqvist, *Phys. Rev. B*, 2001, **64**, 115108.

101 J. L. F. Da Silva, M. V. Ganduglia-Pirovano, J. Sauer, V. Bayer and G. Kresse, *Phys. Rev. B*, 2007, **75**, 045121.

102 M. Petersen, J. Hafner and M. Marsman, *J. Phys.: Condens. Matter*, 2006, **18**, 7021–7043.

103 H. Wang, A. Chroneos and U. Schwingenschlögl, *J. Chem. Phys.*, 2013, **138**, 224705.

104 S. J. Duclos, Y. K. Vohra, A. L. Ruoff, A. Jayaraman and G. P. Espinosa, *Phys. Rev. B*, 1988, **38**, 7755–7758.

105 A. Nakajima, A. Yoshihara and M. Ishigame, *Phys. Rev. B*, 1994, **50**, 13297–13307.

106 L. Gerward, J. S. Olsen, L. Petit, G. Vaitheeswaran, V. Kanchana and A. Svane, *J. Alloys Compd.*, 2005, **400**, 56–61.

107 P. J. Hay, R. L. Martin, J. Uddin and G. E. Scuseria, *J. Chem. Phys.*, 2006, **125**, 034712.

108 J. Kullgren, C. W. M. Castleton, C. Muller, D. M. Ramo and K. Hermansson, *J. Chem. Phys.*, 2010, **132**, 054110.

109 T. Hisashige, Y. Yamamura and T. Tsuji, *J. Alloys Compd.*, 2006, **408–412**, 1153–1156.

110 H. T. Handal and V. Thangadurai, *J. Power Sources*, 2013, **243**, 458–471.

111 S. Sameshima, M. Kawaminami and Y. Hirata, *J. Ceram. Soc. Japan*, 2002, **110**, 597–600.

112 X.-L. Zhao, J.-J. Liu, T. Xiao, J.-C. Wang, Y.-X. Zhang, H.-C. Yao, J.-S. Wang and Z.-J. Li, *J. Electroceramics*, 2012, **28**, 149–157.

113 F. Iguchi, S. Onodera, N. Sata and H. Yugami, *Solid State Ionics*, 2012, **225**, 99 – 103.

114 K. C. Anjaneya, G. P. Nayaka, J. Manjanna, G. Govindaraj and K. N. Ganesha, *J. Alloys Compd.*, 2013, **578**, 53–59.

115 K. Lejaeghere, V. Van Speybroeck, G. Van Oost and S. Cottenier, *Critical Reviews in Solid State and Materials Sciences*, 2014, **39**, 1–24.

116 H. J. Monkhorst and J. D. Pack, *Phys. Rev. B*, 1976, **13**, 5188–5192.

117 F. Deganello and A. Martorana, *J. Solid State Chem.*, 2002, **163**, 527–533.

118 F. Deganello, A. Longo and A. Martorana, *J. Solid State Chem.*, 2003, **175**, 289 – 298.

119 A. R. Denton and N. W. Ashcroft, *Phys. Rev. A*, 1991, **43**, 3161–3164.

120 B. C. Morris, W. R. Flavell, W. C. Mackrodt and M. A. Morris, *J. Mater. Chem.*, 1993, **3**, 1007–1013.

121 V. Bellière, G. Joorst, O. Stephan, F. M. F. de Groot and B. M. Weckhuysen, *J. Phys. Chem. B*, 2006, **110**, 9984–9990.

122 F.-Y. Wang, S. Chen and S. Cheng, *Electrochemistry Communications*, 2004, **6**, 743–746.

123 In *ab-initio* calculations as presented in this work, the oxidation state of the atoms is not strictly defined, and our reference to any type of oxidation state should not be taken as an absolute truth, but rather an educated guess. All elements used as dopants in this work have either a single (most common) oxidation state which is different from IV (*e.g.* Zn) or are multivalent with most common oxidation states different from IV (*e.g.* Yb or V). Since Shannon crystal radii are given both for different coordinations and different oxidation states (although some combinations which might be of interest for this work are missing) we have attempted to derive the oxidation state of the dopants in the presented systems, based on the magnetization of the ground state system, under the assumption of integer values for this magnetization. In most cases these results pointed toward the most common oxidation state, while in other cases degeneracies were present, with Co being the most extreme case (*cf.* Ref. [124]). When the oxidation state was uncertain, Shannon crystal radii in the ball-park of our calculated atomic radii were used as indicator for the dopant oxidation state. As a result, the stated oxidation numbers should only be considered as a guess, although they might point at an underlying physical relation with the atomic oxidation states.

124 Of all systems investigated, Co doping is the most problematic one due to the near degeneracy of different magnetic configurations (magnetization varying from 1 to 5 μ_B show differences in total energy of ~ 0.20 and ~ 0.08 eV for 3% doped systems). Interestingly enough, experiments seem to encounter similar variation in the observed magnetic moment, with values varying with the Co concentration, substrate, and deposition method. Where Tiwari *et al.* present $6\mu_B$ at 3% Co doping, Vodungbo *et al.* measure about $1.5\mu_B$ at 4.5%, while Fernandez *et al.* and Song *et al.* measure about $5\mu_B$ at concentrations of 5 and 3% , respectively. [69–72].

125 B. Cordero, V. Gomez, A. E. Platero-Prats, M. Reves, J. Echeverria, E. Cremades, F. Barragan and S. Alvarez, *Dalton Transactions*, 2008, 2832–2838.

126 A. Ismail, J. Hooper, J. B. Giorgi and T. K. Woo, *Phys. Chem. Chem. Phys.*, 2011, **13**, 6116–6124.

127 R. Lin, M.-F. Luo, Y.-J. Zhong, Z.-L. Yan, G.-Y. Liu and W.-P. Liu, *Appl. Catal., A*, 2003, **255**, 331–336.

128 G. Murgida, V. Vildosola, V. Ferrari and A. Llois, *Solid State Communications*, 2012, **152**, 368–371.

129 N. Van de Velde, T. Bruggeman, L. Stove, G. Pollefeyt, O. Brunkahl and I. Van Driessche, *Eur. J. Inor. Chem.*, 2012, **2012**, 1186–1194.

130 H. Yamamura, H. Nishino and K. Kakinuma, *J. Ceram. Soc. Jpn*, 2004, **112**, 553–558.

131 Y. Tsuru, Y. Shinzato, Y. Saito, M. Shimazu, M. Shiono and M. Morinaga, *J. Ceram. Soc. Jpn.*, 2010, **118**, 241–245.

132 K. Lejaeghere, J. Jaeken, V. Van Speybroeck and S. Cottenier, *Phys. Rev. B*, 2014, **89**, 014304.

133 D. Fagg, J. Frade, V. Kharton and I. Marozau, *J. Sol. State Chem.*, 2006, **179**, 1469–1477.

134 Note that the 'linear' in linear TEC refers to thermal expansion in one dimension, and does not indicate any linearity with regard to this coefficient. Adding to the confusion is the fact that for a large experimental temperature range the coefficient changes roughly linearly, as is shown in Fig. 6.

135 In this, N_{vac} is related to y via the relation $N_{vac} = yN_{uc}$ with N_{uc} the number of unit cells required to build the supercell of the doped system.

136 P. R. L. Keating, D. O. Scanlon, B. J. Morgan, N. M. Galea and G. W. Watson, *J. Phys. Chem. C*, 2012, **116**, 2443–2452.

137 C. Catlow, *Solid State Ionics*, 1983, **8**, 89–107.

138 V. Butler, C. Catlow, B. Fender and J. Harding, *Solid State Ionics*, 1983, **8**, 109–113.

139 F. A. Kröger and H. J. Vink, *Solid State Physics*, 7th edn, 1956, vol. 3.